applied optics

Short dual-core GaAs photonic crystal fiber splitter with a broad bandwidth and ultrahigh extinction ratio

Yanshu Zeng,[1] Jingwei Lv,[1] Lin Yang,[1] Wei Liu,[1] Zao Yi,[2] Qiang Liu,[1] Chunjie Hu,[3] Yan Lv,[1] Paul K. Chu,[4] and Chao Liu[1,*]

[1]School of Physics and Electronic Engineering, Northeast Petroleum University, Daqing 163318, China
[2]Joint Laboratory for Extreme Conditions Matter Properties, Southwest University of Science and Technology, Mianyang 621010, China
[3]Department of Gynecology and Obstetrics, The Fourth Affiliated Hospital of Harbin Medical University, Harbin 150001, China
[4]Department of Physics, Department of Materials Science and Engineering, and Department of Biomedical Engineering, City University of Hong Kong, Tat Chee Avenue, Kowloon, Hong Kong, China
*msm-liu@126.com

Received 16 December 2022; revised 8 February 2023; accepted 13 February 2023; posted 15 February 2023; published 17 March 2023

Microstructured polarization beam splitters (PBSs) have attracted much interest in recent years. Here, a ring double-core photonic crystal fiber (PCB) PSB (PCB-PSB) with an ultrashort, broadband, and high extinction ratio (ER) was designed. The effects of the structural parameters on the properties were analyzed by the finite element method, which revealed that the optimal length of the PSB was 19.08877 μm and the ER was −324.257 dB. The operating bandwidth for an ER of less than −20 dB is 440 nm and the wavelength range spans the full E + S + C + L + U band between 1,320 and 1,760 nm. The fault and manufacturing tolerance of the PBS was demonstrated for structural errors of ±1%. Moreover, the influence of temperature on the performance of the PBS was determined and discussed. Our results show that a PBS has excellent potential in optical fiber sensing and optical fiber communications.

https://doi.org/10.1364/AO.483504

1. INTRODUCTION

In optical communications [1,2], optical routing [3], and photoelectric detection and imaging [4], polarization beam splitters (PBSs) are critical optical devices that divide the incident light into two mutually orthogonal linearly polarized rays along distinct directions [5]. Traditional PBSs typically have prismatic structure such as the Rochon [6] and Wollaston [7] prisms, and thin film interference PBSs [8]. Although most of these PBSs have high extinction ratios (ERs) and simple structures, conventional PBSs are bulky and difficult to integrate. In practice, they often must be connected to optical fibers through photonic integrated circuits. In this respect, miniaturized and integrated optical devices have emerged as a new area of study on the heels of technical advances in microstructured optical devices. An optical fiber PBS [9] has clear advantages such as a small size, compact structure, and compatibility with optical fibers. Nevertheless, PBSs based on conventional single-mode fibers [10,11] have a small birefringence coefficient, which leads to a small ER and a long beam splitter. These issues can be resolved using photonic crystals [12–14], and there is extensive research in fiber [15–17], couplers [18], cavities [19] and the topological photonics field [20]. Photonic crystal fibers (PCFs) have excellent optical properties such as ultrahigh birefringence, tunable dispersion, and cutoff-free single-mode transmission. In addition, a PCF structure can be adjusted and optimized easily; for example, by varying the size, arrangement, spacing, and other characteristics of the cladding pores for a specific application [21,22].

By optimizing the structure, PCF-PBSs can have a short beam splitting length and high ER. In particular, dual-core PCF-PBSs [23,24] have garnered a lot of interest due to favorable birefringence characteristics. Two parallel waveguides can be viewed as dual-core fibers. Mode coupling causes variations in the coupling length of the light energy traveling from one core to another with different polarization directions and separation of light with various polarization directions can be obtained based on this difference. In recent years, many PCF-PBSs have been studied [25–27]. Chen *et al*. [28] proposed a PCF-PBS with hexagonal lattice air holes. This PBS uses fluoride phosphate N-FK51A glass as the bulk material and the outer layer on the central air hole is coated with a high refractive index As_2S_3 film to improve the birefringence. At a wavelength of 1.55 μm, the ER, coupling length, and bandwidth are 83.6 dB, 1 mm, and 280 nm, respectively. Shimu *et al*. [29] reported a dual-core hexagonal PCF-PBS consisting of two parallel golden wires to enhance the coupling strength. At 1.55 μm the coupling

length, ER, and bandwidth of the beam splitter are 481.73, −98 dB, and 200 nm, respectively. Qu *et al*. [30] studied an X-type dual-core PCF-PBS made of Ge20Sb15Se65 glass and, according to the coupling length variation for the two polarization orientations, the PBS coupling length and bandwidth are 230 m and 358 nm, respectively, for a wavelength of 1.55 μm. However, most previously reported PBSs can only satisfy one of the three requirements of a small size, wide bandwidth, and high ER, and only a small number of them can satisfy all the requirements at the same time. Therefore, it is necessary to develop a PCF-PBS that can simultaneously meet all the requirements for miniaturization, a wide bandwidth, and a high ER.

Here, a ring-shape, dual-core PCF-PBS with a simple structure was designed and analyzed. To improve the birefringence of the beam splitter and increase the refractive index difference between the cladding and core, GaAs with a high refractive index was chosen as the substrate. To enhance the asymmetry of the structure, neutral liquid crystal (NLC) was used to fill the central area, which consists of an elliptical hole and eight surrounding larger round holes. Finite element analysis revealed an optimal length of 19.08877 μm, an ER of −324.257 dB, and a bandwidth of 440 nm (ER > 20 dB) at 1.550 μm. This dual-core PCF-PBS not only meets the requirements of miniaturization, a high ER, and a wide bandwidth, but also is simple to produce. Consequently, we believe this PCF-PBS has immense potential in optical communications, optical sensing, and related applications.

2. DESIGN AND BASIC THEORY

Figure 1(a) depicts the cross section of the dual-core PCF-PBS in which the central area comprises an elliptical hole and eight surrounding large holes. The elliptical hole in the central region increases the asymmetry of the fiber structure and produces a strong birefringence effect. The major axis and minor axis of the elliptical hole are b and a, and the radius of the large hole is r_1. The distance between the elliptical hole and large holes is d and the two cores are represented by A and B, respectively. The two layers of air holes in the cladding are arranged circularly to reduce the production complexity. The air holes in the first layer have a radius of r_2 and those in the second layer have a radius of r_3. The blue area in the figure is the perfectly matched layer (PML), which absorbs radiant energy and provides the perfect boundary conditions. The white area represents the air holes, which lower the cladding refractive index and concentrate the light in the core. The gray area is GaAs, which is chosen as the PCF substrate instead of the more common SiO_2 because of the larger refractive index needed to increase the difference in refractive indices between the optical fiber filling materials so that more light is concentrated in the fiber core. The refractive index n_1 of GaAs is determined by the Sellmeier equation [31]

$$n_1(\lambda) = \sqrt{A_1 + \frac{B_1\lambda^2}{\lambda^2 - C^2} + \frac{D\lambda^2}{\lambda^2 - E^2} + \frac{F\lambda^2}{\lambda^2 - G^2}}, \quad (1)$$

where λ is the wavelength of the incident light, $A_1 = 5.372514$, $B_1 = 5.466742\ \mu m^2$, $C = 0.4431307\ \mu m$, $D = 0.2429960\ \mu m^2$, $E = 0.8746453\ \mu m$, $F = 1.957522\ \mu m^2$, and $G = 36.9166\ \mu m$.

The pink area is filled with NCL E7. Compared to other materials, NCL E7 has a high birefringence index in the IR region due to its anisotropy. The refractive index of the fiber background material GaAs is greater than that of NCL, so light can be well confined in the fiber core. The Cauchy formula [32] can be used to calculate the ordinary (n_o) and extraordinary (n_e) refractive indexes, which make up the NCL refractive index:

$$n_{o,e}(\lambda) = A_{o,e} + \frac{B_{o,e}}{\lambda^2} + \frac{C_{o,e}}{\lambda^4}, \quad (2)$$

where $A_{o,e}$, $B_{o,e}$, and $C_{o,e}$ are the coefficients of Cauchy model. A_o, B_o, and C_o are 1.4994, 0.0070 μm^2, and 0.0004 μm^4, respectively, and A_e, B_e, and C_e are 1.6933, 0.0078 μm^2, and 0.0028 μm^4, respectively, at 25°C. The refractive index n_2 of NCL is calculated by

$$n_2 = [n_o, n_e, n_o]. \quad (3)$$

The dual-core PBS can be visualized as two parallel waveguides between which the mode coupling occurs [33–35]. The energy of the two fiber cores is converted as a result of the mode coupling effect when light traverses the fiber core. The operating principle is illustrated in Fig. 1(b). Suppose that a beam of light is incident from core A and transmitted for a distance L. Due to the mode coupling effect, the energy in core A reaches the minimum and the energy in core B reaches the maximum.

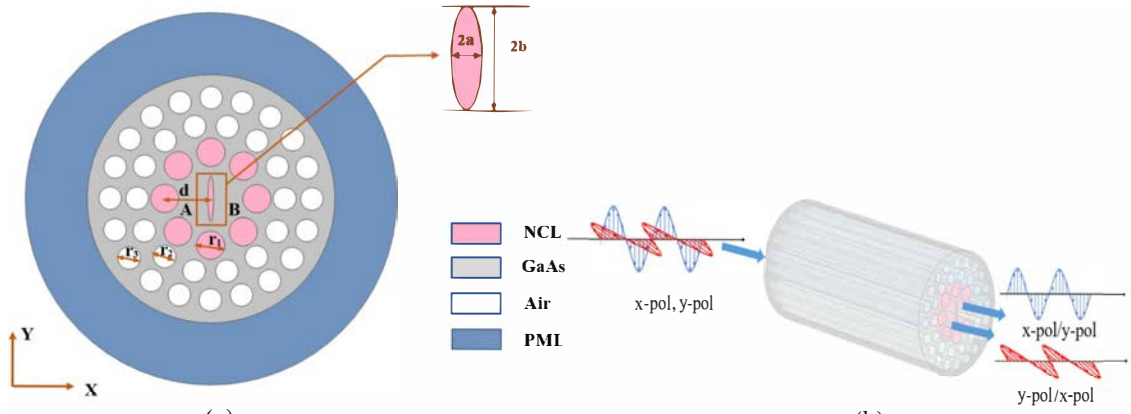

Fig. 1. (a) Cross-section of the PCF-PBS. (b) Schematic showing the PBS operation principle.

According to the different distances when the energy of the light in two polarization directions is completely transferred, we can determine the length of the optical fiber to separate the x- and y-polarized light at the output end of the optical fiber.

The coupling length is one of the important PBS parameters. It describes the shortest transmission distance when the energy exchange occurs between two PBS cores. Therefore, the shorter the coupling length, the better the coupling performance. The coupling lengths of the x and y polarization modes can be calculated by [36]

$$L^{\lambda}_{x(y)} = \frac{\lambda}{2(n^{e}_{x(y)} - n^{o}_{x(y)})}, \tag{4}$$

where $n^{e}_{x(y)}$ is the real part of the effective refractive index of the even mode in the x and y polarization directions, and $n^{o}_{x(y)}$ is the real part of the effective refractive index of the odd mode in the x and y polarization directions. In general, $L_x \neq L_y$ and so the distinct coupling lengths of different polarization directions can be used to separate the beam.

The coupling length ratio (CLR) is an important factor to assess the usability of the PBS and is described by the ratio of L_x to L_y [37]:

$$\mathrm{CLR} = \frac{L_X}{L_y} = \frac{n}{m}, \tag{5}$$

where m and n are positive integers with different parity. The PBS delivers the best performance when CLR is 2 or 1/2 and the length of the PBS satisfies $L = mL_x = nL_y$. The rays in the x and y polarization directions are now entirely separated from one another.

The length of the miniature PCF-PBS has a μm magnitude and the transmission loss can be neglected. The power of the incident light is P_{in} and the output power of the fiber core is P_{out}. The output power in the x and y polarization directions is defined in [38] as

$$P^{x,y}_{\mathrm{out}} = P_{\mathrm{in}}\cos^2\left(\frac{\pi}{2}\frac{L}{L_{x,y}}\right) \tag{6}$$

when the incident light's power is normalized as $P_{\mathrm{in}} = 1$ and the two polarized light normalized power (NP) is expressed by

$$\mathrm{NP} = \frac{P^{x,y}_{\mathrm{out}}}{P_{\mathrm{in}}} = \cos^2\left(\frac{\pi}{2}\frac{L}{L_{x,y}}\right), \tag{7}$$

where L is the PBS length. The normalized power of one polarized light reaches the maximum and that of the other polarized light reaches the minimum at the output of the fiber core.

The degree of separation of the two polarization directions at the fiber output is measured by the ER. The greater the absolute ER, the better the beam separation is. The ER is calculated by [39]

$$\mathrm{ER} = 10\log_{10}\frac{P^{y}_{\mathrm{out}}}{P^{x}_{\mathrm{out}}}, \tag{8}$$

where P^{x}_{out} and P^{y}_{out} are the output power in the x and y polarization directions, respectively. The two polarization states can be distinguished because the output power of the light in the two directions is different by more than 100 times for $|\mathrm{ER}| > 20$ dB. Therefore, we define the bandwidth of the PCF-PBS in the wavelength range when $|\mathrm{ER}| > 20$ dB.

3. RESULTS AND DISCUSSION

According to the supermode theory [40], a dual core fiber has two supermodes: the even supermode and the odd supermode. The even mode has the same electric field direction, whereas the odd mode has opposite electric field directions, as shown in Fig. 2. The four modes, odd in the x and y polarization directions and even in the y and x polarization directions are present in the coupling process of the dual-core PCF as a result of the two polarization directions. Figures 2(c) and 2(d) show the even and odd modes in the x polarization direction and Figs. 2(e) and

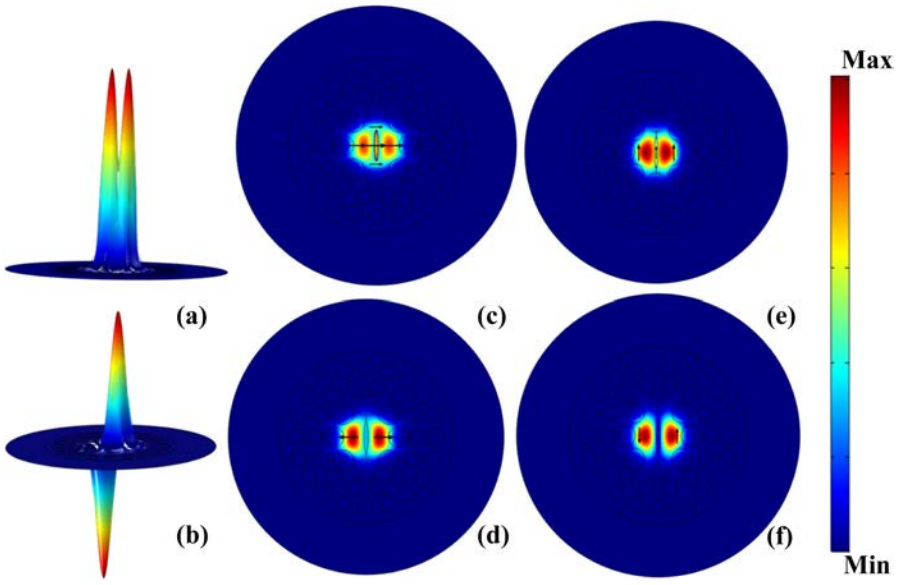

Fig. 2. Electric field distributions: (a) even mode and (b) odd mode. Mode field distributions at 1.55 μm: (c) x polarization even mode, (d) x polarization odd mode, (e) y polarization even mode, and (f) y polarization odd mode.

2(f) are the even and odd modes in the y polarization direction. It can be seen that the light energy is mainly confined to the core.

A. Effects of Structural Parameters

The asymmetry of the core is the main factor affecting the birefringence of PBS and so the size of the cladding air holes and the distance between the air holes have little influence. Here, we mainly optimized the radius r_1 of the large hole, distance d between the large hole and the core, and the parameters of the ellipse. According to previous experience, the initial parameters were set as $a = 0.05$ μm, $b = 0.4$ μm, $r_1 = 0.22$ μm, $d = 0.8$ μm, and $r_2 = r_3 = 0.2$ μm.

Figure 3 exhibits the change of the coupling length and CLR when the distance d between the large round hole and the core is varied while other parameters stay the same. By optimizing d between 0.76 μm to 0.84 μm, a CLR that is infinitely close to 2 or 1/2 was obtained while all the other parameters were constant. In the figure, the black line represents the coupling length in the x polarization direction, the blue line stands for the coupling length in the y polarization direction, and the red curve shows the coupling length ratio. Figure 3 shows that L_x is larger than L_y at the communications wavelength 1.55 μm, indicating that the y-polarized light has a stronger coupling effect. The coupling length increased linearly and the ratio of the coupling length decreased with an increasing d. This shows that when the distance between the large round hole and center increases, the coupling effect decreases. Therefore, PBS performs better when CLR approaches 2 and $d = 0.82$ μm is chosen as the optimal value.

Figure 4 shows the variations in the coupling lengths and CLR with large round hole radii at 1.55 μm. If the radius of the large hole is too large, manufacturing the beam splitter becomes more difficult. However, if the radius is too small, light cannot easily concentrate in the fiber core and so the optimized range of r_1 is between 0.17 μm and 0.25 μm. By keeping the other parameters unchanged, Fig. 4 shows that as r_1 goes up, the coupling length in the x polarization direction (blue curve) and that in the y polarization direction (black curve) decrease gradually. This is because when the radius of the large round hole increases, light can more easily concentrate in the fiber core to enhance the coupling effect. Because L_x decreases faster than L_y, the

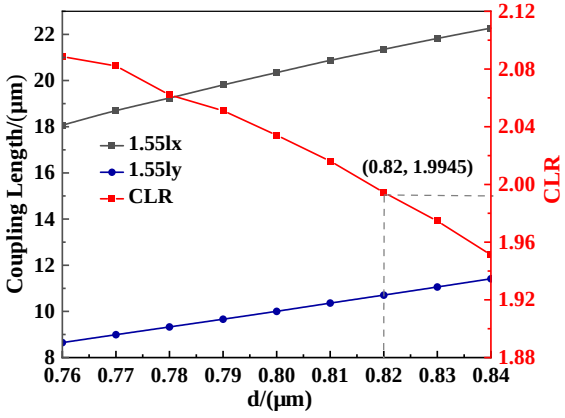

Fig. 3. Coupling lengths and CLR for different distances d between the large round hole and core at 1.55 μm.

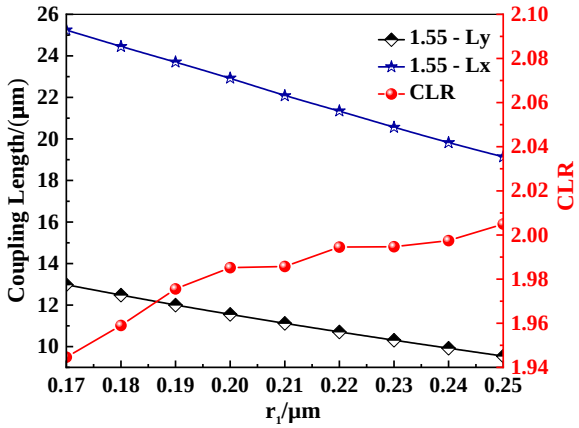

Fig. 4. Relationship between CLR and coupling length with large hole radius.

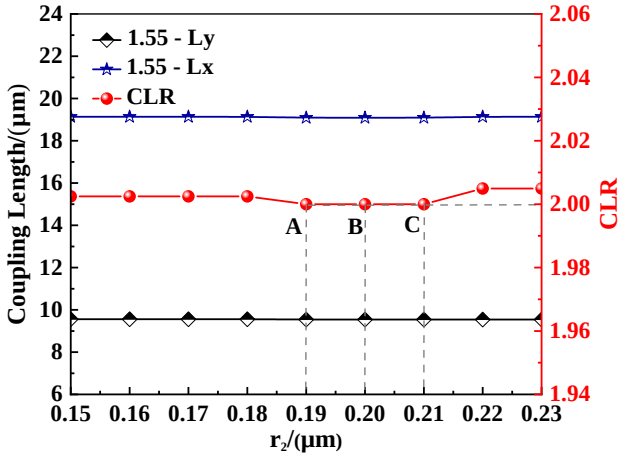

Fig. 5. Effects of the radii of the first-layer air holes on the coupling length and CLR.

CLR rises with increasing r_1 and when $r_1 = 0.25$ μm, the CLR is close to 2, which results in a better performance.

Figure 5 illustrates the trend of the coupling length and CLR when the radii of the air holes in the first layer are changed from 0.15 μm to 0.23 μm. The change has a small effect on the coupling length in the two polarization directions. At points A, B, and C, CLR = 2. This is because the size of the air holes in the first layer barely affects the asymmetry of the fiber core, only slightly altering the coupling strength. Since some manufacturing tolerance must be allowed in actual production, r_2 is determined to be 0.2 μm.

The shape of the ellipse has a notable effect on the polarization beam splitter. Figure 6 shows how the coupling length and CLR are affected by the minor axis of the ellipse. To make CLR close to 2 by optimizing the minor axis of the ellipse, the minor axis a of the ellipse has the range of 0.04 μm to 0.12 μm. Note that if the minor axis is too small and the major axis b is too long, manufacturing and production are difficult. Figure 6(a) shows that as a is increased, the coupling lengths in the two polarization directions increase and the coupling length in the x polarization direction is greater than that in the y polarization direction because the coupling strength weakens as the short

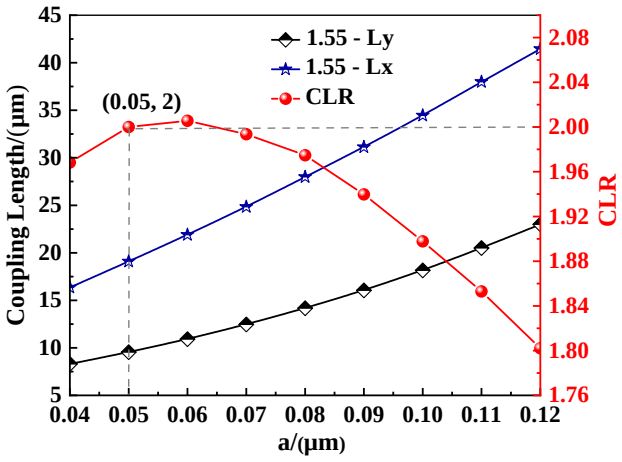

(a)

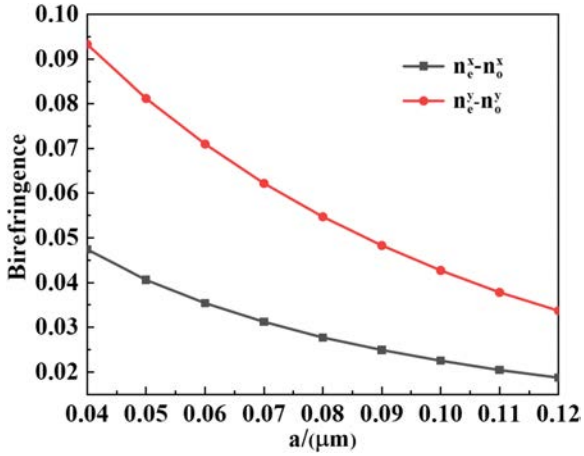

(b)

Fig. 6. Influence of the minor axis on (a) the coupling length and (b) the birefringence.

axis length increases. It can be seen from Fig. 6(b) that with the change in the short axis, the refractive index difference between the odd mode and the even mode in the x and y directions gradually decreases, and the refractive index difference of x polarization is smaller than that of y polarization. According to Eqs. (4) and (5), a change in the minor axis has a greater impact on the y polarization refractive index difference when a is less than 0.06 μm, and a change in the minor axis has a stronger impact on the x polarization refractive index difference when a is bigger than 0.06 μm. Therefore, CLR first magnifies and then diminishes as the minor axis length is increased. For $a = 0.05$ μm, CLR = 2. Figure 7 shows the variation in the coupling lengths and CLR for different major axes of the ellipse between 0.35 μm and 0.43 μm. The coupling length in the x polarization direction goes up with an increase in the major axis b, but the ellipse major axis has little effect on the coupling length in the y polarization direction. The impact of the long axis of the ellipse on birefringence in the x polarization direction is obviously lower than that in the y polarization direction; therefore, CLR goes up with the long axis. For $b = 0.4$ μm, CLR = 2.

According to the aforementioned analysis, the optimal structural parameters of the PCF-PBS are determined to be

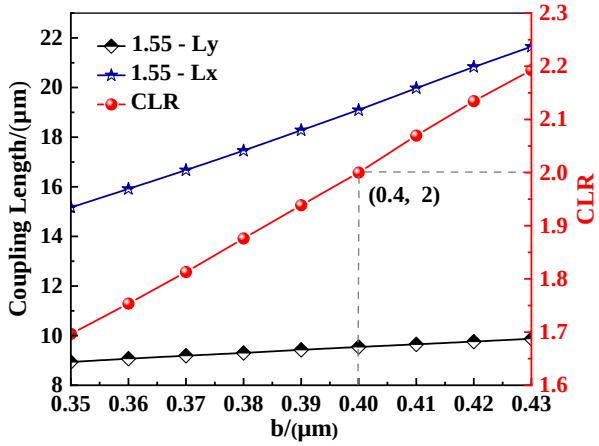

Fig. 7. Influence of the major axis on the coupling length and CLR.

$d = 0.82$ μm, $r_1 = 0.25$ μm, $r_2 = 0.2$ μm, $r_3 = 0.2$ μm, $a = 0.05$ μm, and $b = 0.4$ μm. The coupling lengths in the two polarization directions are $L_x = 19.08867$ μm and $L_y = 9.544335$ μm, and the length of the PCF-PBS is 19.08877 μm.

For the practical production of PBS, we chose the sol-gel method [41] to prepare the PCFs. Compared to other methods, it is easier to control the size, position, and shape of the air hole using this method. The liquid crystal is heated and melted and a syringe is used to put it into the hole.

B. Analysis of the Properties

Figure 8 shows the relationship between the normalized power of the PCF-PBS and the fiber length at 1.55 μm. The red curve represents the normalized power of the x-polarized light in core A and the black curve is the normalized power of the y-polarized light. For different fiber lengths, the optical power of the two polarized lights changes periodically in core A and core B. When the PCF length L is 19.08877 μm, the optical power of the x-polarized light in core A reaches the minimum and the optical power of the y-polarized light is the maximum. Correspondingly, in core B, the optical power of the x-polarized

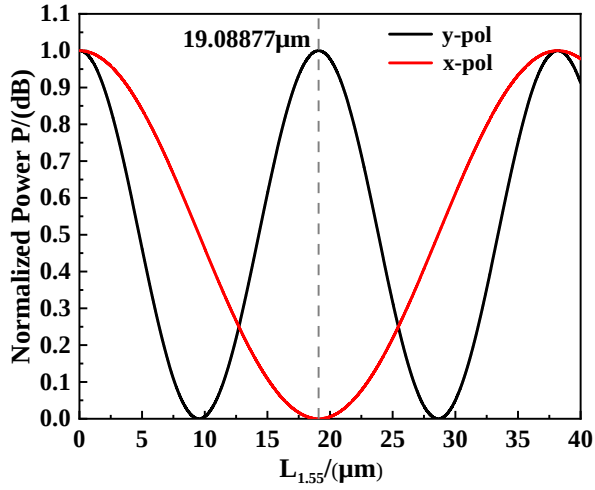

Fig. 8. Relationship between the normalized power $P_{x,y}$ of the PCF-PBS and the fiber length.

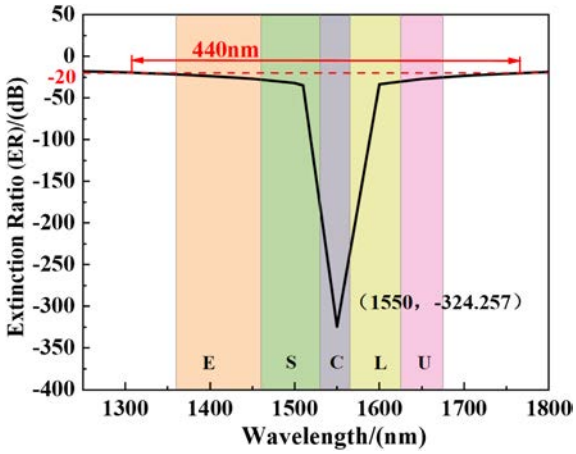

Fig. 9. PCF-PBS ERs.

light is the highest but the optical power of the y-polarized light is the lowest. Therefore, the x-polarized light in core A is completely coupled to core B and the x-polarized light and the y-polarized light can be completely separated.

Figure 9 exhibits the relationship between the ER of the PBS and the incident light wavelength when the incident light wavelength is changed from 1,250 nm to 1,800 nm. The ER is as high as −324.257 dB when the wavelength is 1550 nm. At this time, the output power of the y-polarized light is far less than that of the x-polarized light. The polarized light in two directions is separated. The bandwidth is 440 nm when ER ≤ -20 dB, and the corresponding wavelength range is 1,320–1,760 nm, thus spanning the full E + S + C + L + U band. In optical fiber communications, the wavelength of light affects the transmission loss. The light in the E, S, C and L bands is suitable for transmission in optical fiber due to low signal distortion and minimum loss caused by dispersion. In addition, U band will be mainly used for network monitoring.

C. Fault and Manufacturing Tolerance

Although the optimal structural parameters were determined, tolerance must be provided to allow for errors in the actual production and the impact of ±1% change of the optimal parameters (a, b, r_1, and d) on the performance of the dual-core PBS was analyzed. Figure 10(a) shows the influence of the minor changes in the minor axis a and major axis b of the ellipse on the ER and bandwidth of PCF-PBS. In the gray area, the ER is less than −20 dB. The blue line represents the ER curve for the ideal parameters and small changes in a and b have little effect on the bandwidth. The maximum ER is still 1.55 μm and about 36.89 dB less than the ideal ER when it fluctuates by ±1% (red curve and black dotted line in the figure). When b is increased to 1 + 1% (green curve), the ER shifts to red. The maximum ER is still in the 1.55 μm working wavelength as b is reduced to 1-1%. Figure 10(b) shows that the bandwidth does not change and ER is still the maximum at 1.55 μm when r_1 and d are altered. Together with r_1 increasing by 1%, the ER is only 37.33 dB lower than the ideal value.

Although the change in the structural parameters decreases the ER, the communications bandwidth is almost unaffected when the ER ≤ -20 dB. Therefore, the PCF-PBS still delivers outstanding performance in this communications window.

D. Temperature Effects

The NCL refractive index is affected by temperature [42] and Fig. 11 presents the ER change at 1.55 μm at different temperatures. The temperature change has only a small influence on the bandwidth of the PCF-PBS and the ER is still maximum at 1.55 μm. When the temperature is 25°C, ER is −324.257 dB. In comparison, ER = −54.269 dB at 20°C and −287.623 dB at 30°C. Although the temperature affects the NCL's refractive index and changes the ER, in practice a thermoelectric module can be used to control the temperature [43]. Moreover, GaAs has good heat resistance and small temperature changes have hardly any effect.

E. Performance Comparison

Table 1 lists the main performance indicators of PBSs reported recently in the literature compared to those of our dual-core PCF-PBS in terms of the length, ER, and bandwidth. Note that the optimal structure meets the requirements of miniaturization, high ER, and wide bandwidth, which bodes well for commercial implementation.

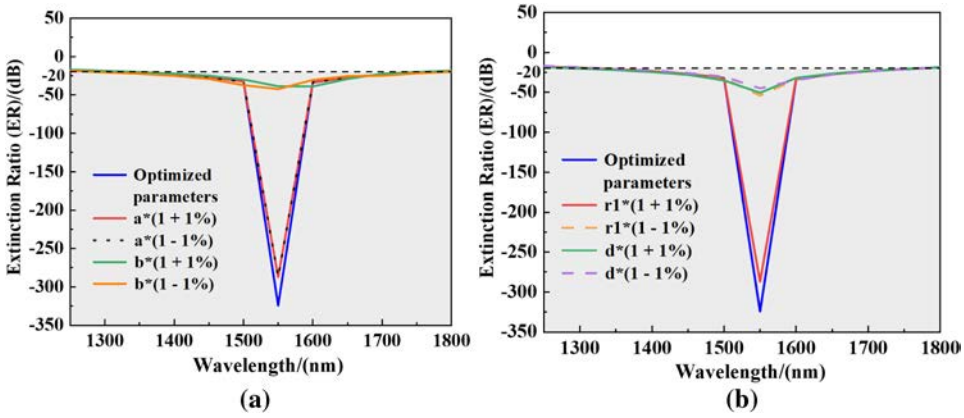

Fig. 10. ER curves for parameter errors within ±1%: (a) error of a and b and (b) error of r_1 and d.

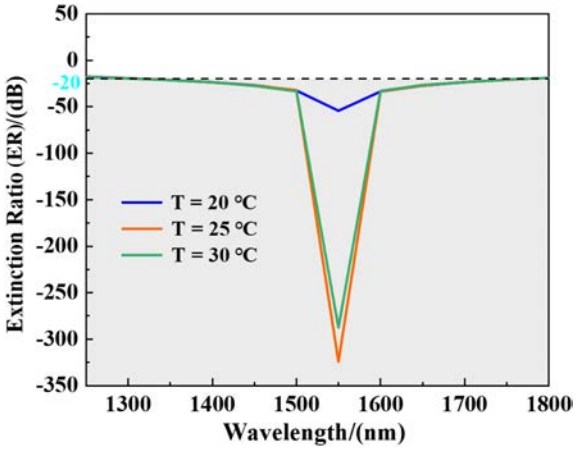

Fig. 11. ER changes at different temperatures.

Table 1. Properties of Recently Reported PBSs vs. Properties of Our PCF-PBS

References	Beam Splitter Length (μm)	ER (dB)	Bandwidth (nm)
[29]	481.73	−98	200
[36]	34	149.9	200
[44]	123.6	78	314
[45]	90.73	109.57	500
[46]	62.5	−71	110
Our work	19.08877	−324.257	440

4. CONCLUSION

An ultrashort, ultrawide bandwidth ring dual-core PCF-PBS was designed and analyzed. The PBS used high-refractive-index GaAs as the bulk materials to enhance the birefringence due to the structural asymmetry. By optimizing the size and spacing of the PCF holes, the optimal structural parameters were derived for a coupling length ratio of 2. The influence of the structural parameters on the coupling characteristics was determined to optimize the structure. Finite element analysis revealed that the optimal PBS length is 19.08877 μm, the ER is −324.257 dB, and the bandwidth is 440 nm. The PBS performed well and its bandwidth was unaffected despite changes in the ERs. To demonstrate the high tolerance, the properties of the device were maintained even when the structural parameters were changed by ±1% to simulate manufacturing errors and operating temperature fluctuations. Furthermore, the dual-core PCF-PBS has a simple structure, which makes it simple to manufacture while simultaneously meeting the three key requirements: an ultrashort length, a high ER, and a wide bandwidth. These advantages suggest that the dual-core PCF-PBS has good application prospects in many areas.

Funding. Outstanding young and middle-aged research and innovation team of Northeast Petroleum University (KYCXTD201801); Local Universities Reformation and Development Personnel Training Supporting Project from Central Authorities, Natural Science Foundation of Heilongjiang Province (LH2021F007); China Postdoctoral Science Foundation (2020M670881); City University of Hong Kong Strategic Research Grant (SRG) (7005505); City University of Hong Kong Donation Research Grant (DON-RMG No. 9229021); Scientific Research Fund of Sichuan Province Science and Technology Department (2020YJ0137).

Disclosures. The authors declare no conflicts of interest.

Data availability. Data underlying the results presented in this paper are not publicly available at this time but may be obtained from the authors upon reasonable request.

REFERENCES

1. M. T. H. Azar, H. Alipour-Banaei, and M. Zavvari, "A high efficiency optical power splitter in a y-branch photonic crystal for DWDM optical communication systems," Frequenz **72**, 79–84 (2018).
2. J. Sharma, R. Sharma, and L. K. Dusad, "Review and analysis of photonic crystal beam splitters for optical communication applications," in *International Conference on Green Computing and Internet of Things (ICGCIoT)* (IEEE, 2015).
3. T. H. Qiu, H. Li, M. Xie, Q. Liu, H. Y. Ma, and R. Xu, "Efficient all-optical router and beam splitter for light with orbital angular momentum," Opt. Express **28**, 19750–19759 (2020).
4. Y. Zhai, F. Wang, Y. Chi, and K. Cen, "Optical absorption tomography for temperature and H_2O concentration imaging by a compact photoelectric detecting system combined with twice adaptive algebraic algorithm," Opt. Eng. **61**, 034103 (2022).
5. A. Herrero-Bermello, A. Dias-Ponte, J. M. Luque-González, A. Ortega-Moñux, A. V. Velasco, P. Cheben, and R. Halir, "Experimental demonstration of metamaterial anisotropy engineering for broadband on-chip polarization beam splitting," Opt. Express **28**, 16385–16393 (2020).
6. B. Wang, F. Dong, H. Feng, D. Yang, Z. Song, L. Xu, W. Chu, Q. Gong, and Y. Li, "Rochon-prism-like planar circularly polarized beam splitters based on dielectric metasurfaces," ACS Photon. **5**, 1660–1664 (2017).
7. M. W. Kudenov, M. Miskiewicz, N. Sanders, and M. J. Escuti, "Achromatic Wollaston prism beam splitter using polarization gratings," Opt. Lett. **41**, 4461–4463 (2016).
8. J. A. Dobrowolski, "Review of thin film interference polarizers and polarizing beam splitters for the visible and adjacent spectral regions," in *Optical Interference Coatings* OSA Technical Digest Series (Optica Publishing Group, 2001), paper FB1.
9. E. A. A. Hagras, M. F. O. Hameed, and S. S. A. Obayya, "Compact dual-core liquid crystal photonic crystal fiber polarization splitter for terahertz applications," Optik **265**, 169396 (2022).
10. H. Jia, X. Wang, T. Zhao, Z. Tang, Z. Lian, S. Lou, and X. Sheng, "Ultrawide bandwidth single-mode polarization beam splitter based on dual-hollow-core antiresonant fiber," Appl. Opt. **60**, 9781–9789 (2021).
11. P. A. Mohammed, "Integration of self-standing X- and Y-shaped polymer coupler and splitter with single mode optical fibers," Opt. Mater. **111**, 110685 (2021).
12. Q. Xu, Y. Peng, B. Yan, A. Shi, P. Peng, J. Xie, and J. Liu, "Multiband topological states in the Penrose-triangle photonic crystals," Opt. Lett. **48**, 101–104 (2023).
13. B. Yan, Y. Peng, A. Shi, J. Xie, P. Peng, and J. Liu, "Pseudo-spin-valley coupled topological states protected by different symmetries in photonic crystals," Opt. Lett. **47**, 2044–2047 (2022).
14. Y. Peng, E. Liu, B. Yan, J. Xie, A. Shi, P. Peng, H. Li, and J. Liu, "Higher-order topological states in two-dimensional Stampfli-Triangle photonic crystals," Opt. Lett. **47**, 3011–3014 (2022).
15. C. Li, B. Yan, and J. Liu, "Refractive index sensing characteristics in a D-shaped photonic quasi-crystal fiber sensor based on surface plasmon resonance," J. Opt. Soc. Am. A **36**, 1663–1668 (2019).
16. B. Yan, A. Wang, E. Liu, W. Tan, J. Xie, R. Ge, and J. Liu, "Polarization filtering in the visible wavelength range using surface plasmon resonance and a sunflower-type photonic quasi-crystal fiber," J. Phys. D **51**, 155105 (2018).
17. E. Liu, S. Liang, and J. Liu, "Double-cladding structure dependence of guiding characteristics in six-fold symmetric photonic quasi-crystal fiber," Superlattices Microstruct. **130**, 61–67 (2019).
18. M. Yuan, X. Han, H. Xiao, T. G. Nguyen, A. Boes, G. Ren, Q. Hao, J. Xue, A. Mitchell, and Y. Tian, "Integrated lithium niobate polarization beam splitter based on a photonic-crystal-assisted multimode interference coupler," Opt. Lett. **48**, 171–174 (2023).

19. R. Ge, X. Yan, Z. Liang, H. Li, J. Wu, X. Liu, Y. Chen, and X. Chen, "Large quality factor enhancement based on cascaded uniform lithium niobate bichromatic photonic crystal cavities," Opt. Lett. **48**, 113–116 (2023).
20. P. Peng, E. Liu, B. Yan, Y. Peng, A. Shi, J. Xie, H. Li, Y. Xiang, and J. Liu, "Pair-partitioned bulk localized states induced by topological band inversion," Appl. Phys. Lett. **121**, 011103 (2022).
21. W. Liu, C. Hu, L. Zhou, Z. Yi, C. Liu, J. Lv, L. Yang, and P. Chu, "A square-lattice D-shaped photonic crystal fiber sensor based on SPR to detect analytes with large refractive indexes," Phys. E **138**, 115106 (2022).
22. H. Fu, Y. Shi, Z. Yi, C. Liu, X. Song, J. Lv, L. Yang, and P. Chu, "Effects of air holes in the cladding of photonic crystal fibers on dispersion and confinement loss of orbital angular momentum modes," Opt. Quantum Electron. **54**, 1–17 (2022).
23. S. Jegadeesan, M. Dhamodaran, M. Azees, and A. Murugan, "Design of a polarization splitter based on a dual-core hexagonal-shaped photonic crystal fiber," Curr. Opt. Photon. **3**, 304–310 (2019).
24. V. Kumar, R. K. Varshney, and S. Kumar, "Design of a compact and broadband terahertz polarization splitter based on gradient dual-core photonic crystal fiber," Appl. Opt. **59**, 1974–1979 (2022).
25. J. X. Zhang, "Dual-core PCF-based THz polarization beam splitter with broad bandwidth and ultra-high extinction ratio," Optik **251**, 168425 (2022).
26. N. Gómez-Cardona, C. Jiménez-Durango, J. Usuga-Restrepo, P. Torres, and E. Reyes-Vera, "Thermo-optically tunable polarization beam splitter based on selectively gold-filled dual-core photonic crystal fiber with integrated electrodes," Opt. Quantum Electron. **53**, 1–15 (2021).
27. A. Bertoncini and C. Liberale, "3D-printed ultrashort and broadband polarizing beam splitter based on PCF design," Proc. SPIE **11682**, 116820G (2021).
28. N. Chen, X. Zhang, X. Lu, Z. Zhang, Z. Mu, and M. Chang, "Numerical investigation of a short polarization beam splitter based on dual-core photonic crystal fiber with As_2S_3 layer," Micromachines **11**, 706 (2020).
29. S. Shimu and M. T. B. Shawkat, "A polarization splitter using dual core photonic crystal fiber," in *International Conference on Automation, Control and Mechatronics for Industry 4.0 (ACMI)* (IEEE, 2021), pp. 1–6.
30. Y. Qu, J. Yuan, K. Wang, S. Qiu, X. Zhou, B. Yan, Q. Wu, B. Liu, K. Wang, X. Sang, K. Long, and C. Yu, "$Ge_{20}Sb_{15}Se_{65}$ glass-based ultra-bandwidth X-shaped dual-core photonic crystal fiber polarization beam splitter with an air hole filled gold rod," J. Opt. Soc. Am. B **39**, 1580–1589 (2022).
31. F. Wang, Y. Chen, C. Li, T. Ma, X. Wang, K. Yu, and L. Li, "Ultracompact and broadband mid-infrared polarization beam splitter based on an asymmetric directional coupler consisting of $GaAs_2$ hybrid plasmonic waveguide and GaAs-CaF_2 nanowire," Opt. Commun. **502**, 127418 (2022).
32. Y. Qu, Y. Han, J. Yuan, X. Zhou, B. Yan, K. Wang, X. Sang, and C. Yu, "A novel liquid crystal-filled, dual-core photonic crystal fiber polarization beam splitter covering the E+ S+ C+ L+ U communication band," Photonics **8**, 461 (2021).
33. H. Zhao and H. Li, "Advances on mode-coupling theories, fabrication techniques, and applications of the helical long-period fiber gratings: a review," Photonics **8**, 106 (2021).
34. X. Wang, J. Zhang, J. Zhu, Z. Yi, and J. Yu, "Refractive index sensing of double Fano resonance excited by nano-cube array coupled with multilayer all-dielectric film," Chin. Phys. B **31**, 024210 (2021).
35. H. Chen, Z. Chen, H. Yang, L. Wen, Z. Yi, Z. Zhou, B. Dai, J. Zhang, X. Wu, and P. Wu, "Multi-mode surface plasmon resonance absorber based on dart-type single-layer graphene," RSC Adv. **12**, 7821–7829 (2022).
36. A. A. Revathi and D. Rajeswari, "Design of polarization splitter based on dual-core surface plasmon resonance photonic crystal fiber," Eur. Phys. J. D **76**, 1–8 (2022).
37. E. A. A. Hagras, M. F. O. Hameed, A. M. Heikal, and S. S. A. Obayyabe, "Multi-functional photonic crystal fiber splitter for the two communication bands," Opt. Fiber Technol. **52**, 101986 (2019).
38. M. T. Rahman and A. Khaleque, "Ultra-short polarization splitter based on a plasmonic dual-core photonic crystal fiber with an ultra-broad bandwidth," Appl. Opt. **58**, 9426–9433 (2019).
39. Y. Zhang, Y. Qu, J. Yuan, H. Wang, X. Zhou, and J. Huo, "Polarization beam splitter based on the gold wire-filled dual-core photonic crystal fiber at the communication wavelengths," Fiber Integr. Opt. **40**, 70–83 (2021).
40. X. Yu, M. Liu, Y. Chung, M. Yan, and P. Shum, "Coupling coefficient of two-core microstructured optical fiber," Opt. Commun. **260**, 164–169 (2006).
41. M. S. Islam, S. Rana, M. R. Islam, M. Faisal, H. Rahman, and J. Sultana, "Porous core photonic crystal fibre for ultra-low material loss in THz regime," IET Commun. **10**, 2179–2183 (2016).
42. J. Li, S. T. Wu, and S. Brugioni, "Infrared refractive indices of liquid crystals," J. Appl. Phys. **97**, 073501 (2005).
43. S. An, Y. Shi, Z. Yi, C. Liu, T. Sun, J. Lv, L. Yang, and P. Chu, "Ultra-short dual-core GaAs photonic crystal fiber splitter filled with nematic liquid crystal," Opt. Eng. **60**, 056104 (2021).
44. C. Mei, Y. Wu, J. Yuan, S. Qiu, and X. Zhou, "Design of compact and broadband polarization beam splitters based on surface plasmonic resonance in photonic crystal fibers," Micromachines **13**, 1663 (2022).
45. M. T. Rahman, A. Khaleque, F. Rabbi, and M. Rahman, "Polarization beam splitter on metal nanowires filled micro-structured optical fiber," in *3rd International Conference on Electrical, Computer & Telecommunication Engineering (ICECTE)* (IEEE, 2019), pp. 137–140.
46. K. Wang, Y. Qu, J. Yuan, S. Qiu, X. Zhou, B. Yan, Q. Wu, B. Liu, K. Wang, X. Sang, and C. Yu, "Ultra-short polarization beam splitter based on dual-core photonic crystal fiber with surface plasmon resonance effect," Opt. Eng. **60**, 076104 (2021).